Supplementary Information for

Spatiotemporal Photothermal Modulation Microscopy (SPM^2) for High-sensitivity Deep-subwavelength Defect Inspection

Jinsong Zhang[1], Xinping Ouyang[1], Kuo Yang[1], Wei Wang[1], Hao Jiang[1], Jian Wang[1], Shuming Yang[2], Jinlong Zhu[1,3,*], Shiyuan Liu[1,*]

[1] School of Mechanical Science and Engineering, Huazhong University of Science and Technology, Wuhan 430074, China.

[2] State Key Laboratory for Manufacturing System Engineering, Xi'an Jiaotong University, Xi'an 710049, China.

[3] Research Institute of Huazhong University of Science and Technology Shenzhen, Shenzhen 518057, China.

[*]Email: jinlongzhu03@hust.edu.cn and shyliu@hust.edu.cn.

Contents

S1. Optical properties of silicon at elevated temperatures. (Figure S1)

S2. Optical cross-section calculation. (Figure S2)

S3. Excited thermal field simulation through heat transfer. (Figure S3)

S4. Optical far-field imaging calculation using a vector diffraction imaging model. (Figure S4)

S5. Temperature dependence of defect inspection. (Figure S5)

S6. Photograph of the experimental photothermal-enhanced defect inspection setup. (Figure S6)

S7. The flowchart for fabricating the patterned SOI wafer. (Figure S7)

S8. Experimental evaluation of pump-beam power density. (Figure S8)

S9. SEM verification of structural integrity after pump-excitations. (Figure S9)

S10. Stitched scanning and contrast enhancement under non-uniform thermal conditions. (Figure S10)

S11. Experimental signal-to-noise ratio analysis of defect perturbation signals. (Figure S11)

References

S1. Optical properties of silicon at elevated temperatures

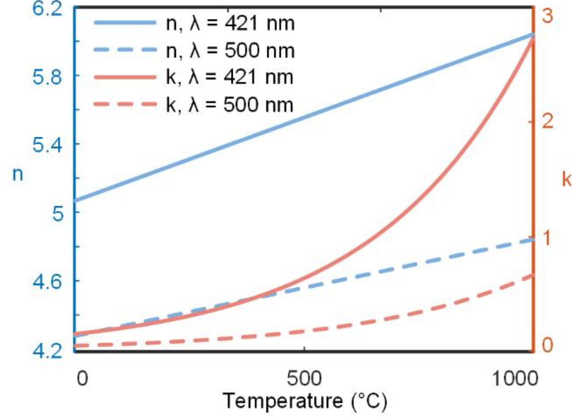

Figure S1. Temperature dependence of the optical constants *n* and *k* of crystalline silicon at critical wavelengths 421nm and 500nm.

The electromagnetic simulations leverage the thermo-optic effect in crystalline silicon, where temperature-dependent optical constants enable modulation of photothermal scattering. This critical response originates from bandgap narrowing, lattice thermal expansion, and electronic polarizability. We utilize the empirical analytical expressions proposed by Jellison and Modine, which characterize the optical functions of silicon at different temperature[1,2]. The refractive index n (E_e, T) is fitted using a linear model dependent on temperature:

$$n(E_e, T) = n_0(E_e) + \alpha(E_e) * T \tag{S1}$$

Here, T is the temperature in °C, and E_e is the photon energy in eV. The functions n_0 (E_e) and α (E_e) are given by the following expressions:

$$n_0 = (4.565 + 97.3 / (3.648^2 - E_e^{\,2}))^{0.5} \tag{S2a}$$

$$\alpha = (-1.864 + 53.94 / (3.648^2 - E_e^{\,2})) * 10^{-4} \tag{S2b}$$

The extinction coefficient k (E_e, T) is fitted using an exponential model dependent on temperature:

$$k(E_e, T) = k_0(E_e) \cdot \exp(\frac{T}{T_0(E_e)}) \quad \text{(S3)}$$

The expressions for the functions $k_0(E_e)$ and $T_0(E_e)$ are:

$$k_0(E_e) = -0.0805 + \exp(-3.1893 + 7.946 / (3.648 \wedge 2 - E_e^{\ 2})) \quad \text{(S4a)}$$

$$T_0(E_e) = 369.9 - \exp(-12.92 + 5.509 * E_e) \quad \text{(S4b)}$$

Integrating these expressions into the FDTD simulation allows us to accurately model the dynamic change in the optical constants of the nanopatterns under pump-excitation. The calculated optical constants of silicon at 25 °C and 500 °C are presented in Fig. 2a. The specific values of the optical constants at the pump wavelength 421 nm and near the resonance band 500 nm are shown in Fig. S1.

S2. Optical Cross-Section calculation

The interaction of an electromagnetic field with a nanopattern redistributes energy through scattering, absorption, and transmission. The total energy loss from the incident wave, termed extinction P_{ext}, is the sum of scattering P_{sca} and absorption P_{abs}. The intensity of the scattering field is determined by the illumination intensity and the nanostructure’s scattering efficiency[3]. The scattering cross-section σ_{sca} is the parameter used to quantify the nanostructure's scattering efficiency, which follows the relationship:

$$P_{sca} = \sigma_{sca} \cdot I_{PD} \quad \text{(S5)}$$

Here, P_{sca} is the power of the light-field scattered by the nanostructure into all directions, and I_{PD} is the power density of the illumination field (in W m^{-2}). P_{sca} can be obtained by integrating the Poynting vector of the scattered far-field over a closed surface:

$$P_{\rm sca} = \iint_{4\pi} \frac{1}{2} \mathrm{Re}(\boldsymbol{E}_{\rm sca} \times \boldsymbol{H}^{*}_{\rm sca}) \cdot \hat{\boldsymbol{r}} \cdot r^2 d\Omega \qquad \text{(S6)}$$

Here, $E_{\rm scat}$ and $H_{\rm sca}$ denote the scattered electric and magnetic fields, respectively, * is the complex-conjugate operator, Re takes the real part, $\hat{\boldsymbol{r}}$ is the unit vector in the scattering direction, and $r^2 d\Omega$ is the elemental area of the spherical surface, with the integration spanning the entire 4π solid angle.

A portion of the energy from the excited polarization currents within the nanostructure is converted to thermal energy via resistive losses and electron-phonon coupling, resulting in optical energy absorption. The absorption cross-section $\sigma_{\rm abs}$ is the parameter used to describe the nanostructure's absorption efficiency, defined by the relationship:

$$P_{\rm abs} = \sigma_{\rm abs} \cdot I_{\rm PD} \qquad \text{(S7)}$$

where $P_{\rm abs}$ is the absorbed power by the nanostructure. The absorbed power $P_{\rm abs}$ is related to the imaginary part of the material's permittivity ε'', and is calculated by:

$$P_{abs} = \iiint_{V} \pi f \varepsilon_0 \varepsilon'' \left| \boldsymbol{E}_V \right|^2 dV \qquad \text{(S8)}$$

Here, f is the frequency of the illumination field, ε_0 is the permittivity of free space, $E_{\rm v}$ is the local electric field within the nanostructure, and dV is the volume element. The extinction cross-section $\sigma_{\rm ext}$ is the sum of the scattering and absorption cross-sections, quantifying the ratio of energy lost by the incident field in the propagation direction:

$$\sigma_{\rm ext} = \sigma_{\rm sca} + \sigma_{\rm abs} \qquad \text{(S9)}$$

These cross-sections form the quantitative basis for understanding the photothermal modulation of scattering contrast presented in the main text. We employed the FDTD software package to calculate the scattering and absorption cross-sections of the silicon nanostructures at different temperatures. In the simulation model shown in Fig. S2, a Total-Field Scattering-Field (TFSF)

source was utilized. The TFSF source separates the incident field from the scattered field by defining a total-field region and injecting the illumination field at its boundaries[4]. A closed scattering-field monitor is placed in the scattering-field region to capture the scattered field distribution. Integration of this field distribution yields the total scattered energy and the corresponding scattering cross-section σ_{sca}. To calculate the absorption cross-section σ_{abs}, a set of absorption field monitors is placed within the total-field region, completely enclosing the nanostructure. The energy flux recorded by these monitors corresponds to the absorption of incident light by the nanostructure. Integrating the electromagnetic fields from this distribution yields the absorbed energy P_{abs} and the absorption cross-section σ_{abs}. Furthermore, we refined the scattering field monitors: those above the nanostructure collect the backward-scattered field (yielding the backward scattering cross-section, $\sigma_{sca\text{-}b}$), while those below collect the forward-scattered field (yielding $\sigma_{sca\text{-}f}$), corresponding to reflection- and transmission-mode imaging, respectively. Given that reflection mode is standard in wafer inspection, we focus our analysis on $\sigma_{sca\text{-}b}$.

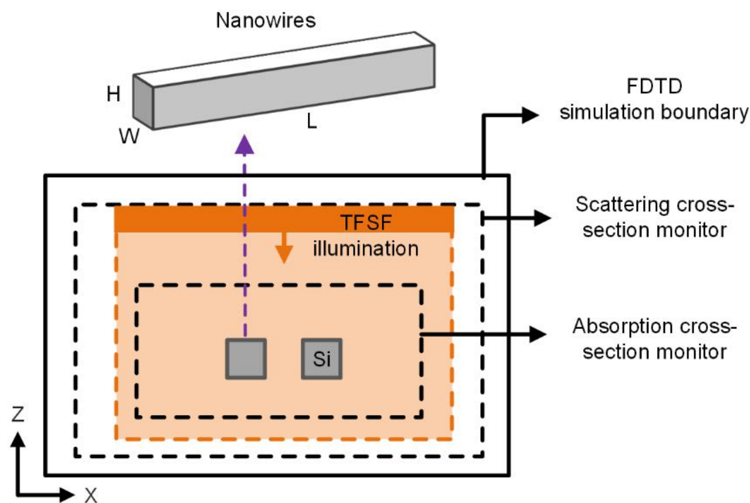

Figure S2. Schematic diagram of the FDTD model for calculating the cross-sections of nanopatterns on the SOI wafer.

S3. Excited thermal field simulation through heat transfer

A 3D solid heat transfer model was built using a finite-element heat transfer solver to simulate the temperature field distribution, as illustrated in Fig. S3a. The dimensions of the nanowires are identical to those used in Fig. 2b. The bottom is bulk single-crystal silicon, the top layer is patterned single-crystal silicon nanowires, and the 1 μm thick middle layer is thermal-grown amorphous silicon dioxide[5,6]. The air domain above the structure was modeled as a stationary fluid, considering heat transfer solely through conduction. For accurate steady-state and transient thermal calculations, we used a simulation domain sufficiently large to avoid boundary effects on the nanostructure temperature field. The final dimensions were: 2 μm (air), 1 μm (Si substrate), and 6 μm × 6 μm (lateral). The thermal properties of all simulated materials are listed in Table S1. The top and bottom Boundaries are set to 25 °C boundary conditions, and four Lateral Boundaries are Heat Flux boundary conditions. In this configuration, the generated heat is predominantly dissipated through the substrate because the thermal conductivity of Si and SiO_2 is much higher than that of air. The heat source term Q (the absorbed optical power density in W m^{-3}) is applied volumetrically within the silicon nanostructure, which is expressed by

$$Q = \frac{\sigma_{abs}(T) \cdot I_{PD}}{V} \tag{S10}$$

Here, V is the nanowire's volume. Crucially, the absorption cross-section σ_{abs} is temperature-dependent $\sigma_{abs}(T)$, determined by interpolating the curves in Fig. 2h based on the calculated average nanowire temperature. The calculated cross-sectional temperature field for $I_{PD} = 1.7*10^9$ W m^{-2} is shown in Fig. S3b. The temperature decreases near the edges, which is attributed to finite-domain boundary effects.

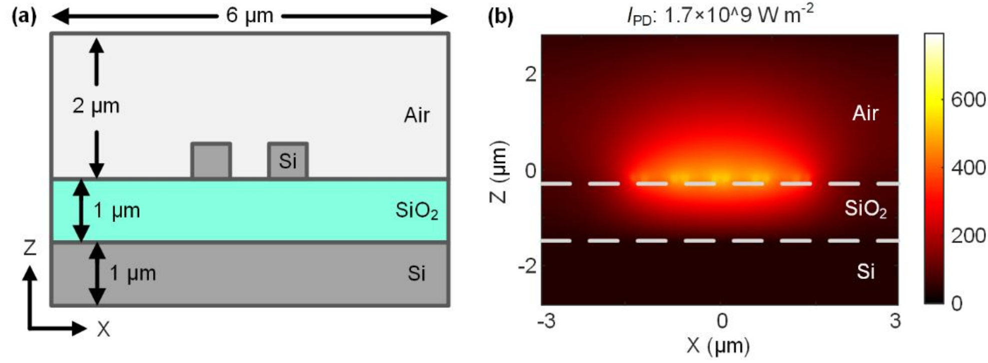

Figure S3. Heat transfer simulation model and results for the nanopattern. (a) Schematic diagram of the heat transfer simulation model. (b) Steady-state cross-sectional thermal field distribution.

Table S1. Thermophysical properties of materials used in the simulations.

Material	Heat conductivity k: W m$^{-1}\cdot$K^{-1}	Heat capacity Cp: J kg$^{-1}\cdot$K^{-1}	Density ρ: kg m^{-3}
SiO_2 (Amorphous)	1.3	703	2200
Si (Crystalline)	140	700	2330
Air	0.026	1005	1.19

To evaluate the sensitivity to thermal boundary conditions, additional simulations were performed. The convective heat transfer coefficient at the lateral boundaries was varied within a typical natural convection range (h = 2-20 W m$^{-2}\cdot$K^{-1}), and the resulting temperature fields were nearly identical. We also varied the Si substrate thickness from 1 µm to 10 µm, resulting in peak temperatures ranging from 527.14 °C to 534.63 °C (variation ~1.4%). In addition, doubling the lateral dimension of simulating region produced a peak temperature of 528.66 °C. These results indicate that the simulated temperature field is weakly sensitive to the boundary conditions within the investigated range.

S4. Optical far-field imaging calculation using a vector diffraction imaging model

The near-field scattering from the nanostructures on a SOI substrate was simulated using an FDTD solver. A plane-wave source was placed 0.3 μm above the substrate, and a field monitor was positioned at 0.45 μm to collect the near-field data, with perfectly matched layers (PMLs) applied to all six boundaries. This near-field data was then propagated to the far-field using an in-house MATLAB-based vector diffraction model to simulate the images captured by the camera, as shown in Fig. S4.

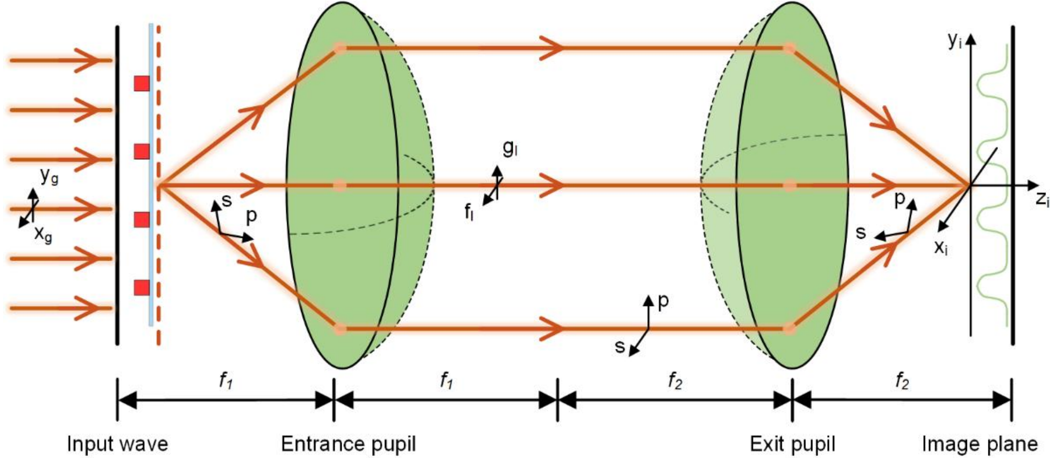

Figure S4. Schematic of the vector diffraction imaging model. A plane wave illuminates the nanostructures, producing a scattered field that the entrance pupil of a projection system collects. The field propagates to the exit pupil, where an inverse Fourier transform is applied to form the final image.

The initial field $\boldsymbol{E}_{\text{in}}$ entering the imaging projection system is acquired directly from the FDTD simulation of the nanostructure's near-field distribution, defined as:

$$\boldsymbol{E}_{\text{in}} = \begin{bmatrix} E_{\text{NF-x}} & E_{\text{NF-y}} & E_{\text{NF-z}} \end{bmatrix}^{\text{T}} \tag{S11}$$

To adequately describe the light-field in the Fourier domain, a local Cartesian coordinate system is defined for both the entrance and exit pupils. The coordinates are expressed as:

$$\begin{aligned} &\alpha_{\text{en}} = \sin\theta_{\text{in}}\cos\varphi_{\text{in}}, \quad \beta_{\text{en}} = \sin\theta_{\text{in}}\sin\varphi_{\text{in}}, \quad \gamma_{\text{en}} = \cos\theta_{\text{in}} \\ &\alpha_{\text{ex}} = \frac{\alpha_{\text{en}}}{M}, \quad \beta_{\text{ex}} = \frac{\beta_{\text{en}}}{M}, \quad \gamma_{\text{ex}} = \sqrt{1-\alpha_{\text{ex}}^2-\beta_{\text{ex}}^2} \end{aligned} \tag{S12}$$

where θ_{in} and φ_{in} represent the incidence angle and azimuth angle of the wave vector, respectively. The orthogonal coordinates are denoted by α, β, and γ, with subscripts en and ex distinguishing the entrance and exit values. M is the magnification of the projection system. The propagation of the light wave from the input plane to the entrance pupil plane is described by the transformational matrix $\boldsymbol{T}_{\text{en}}$, which is written as[7]

$$\boldsymbol{T}_{\text{en}} = \begin{bmatrix} \dfrac{-\beta_{\text{en}}}{\sqrt{\alpha_{\text{en}}^2+\beta_{\text{en}}^2}} & \dfrac{\alpha_{\text{en}}}{\sqrt{\alpha_{\text{en}}^2+\beta_{\text{en}}^2}} \\ \dfrac{-\alpha_{\text{en}}}{\gamma_{\text{en}}\cdot\sqrt{\alpha_{\text{en}}^2+\beta_{\text{en}}^2}} & \dfrac{-\beta_{\text{en}}}{\gamma_{\text{en}}\cdot\sqrt{\alpha_{\text{en}}^2+\beta_{\text{en}}^2}} \end{bmatrix} \tag{S13}$$

The imaging system's inherent Fourier domain cutoff is accounted for by implementing a window function $\boldsymbol{W}$ that is expressed as

$$\boldsymbol{W} = \begin{cases} 1 & (\alpha_{\text{en}}^2+\beta_{\text{en}}^2)/(NA\cdot M)^2 \leq 1 \\ 0 & \text{others} \end{cases} \tag{S14}$$

where NA is determined by the objective lens in the projection system. The electric field, $\boldsymbol{E}_{en}$ at the entrance pupil plane, after the application of the window function, is thus defined as:

$$\boldsymbol{E}_{\text{en}}(\alpha_{\text{en}},\beta_{\text{en}},\gamma_{\text{en}}) = T_{\text{en}}\cdot\frac{\gamma_{\text{en}}}{i\cdot\lambda}\cdot\frac{\exp(i\cdot 2\pi\cdot r_{\text{en}})}{r_{\text{en}}}\cdot f(\boldsymbol{E}_{\text{in}})\cdot\boldsymbol{W}(\alpha_{\text{en}},\beta_{\text{en}}) \tag{S15}$$

Here, r_{en} represents the distance between the source point in the input field and the image point in the entrance pupil plane. Subsequently, the field propagates toward the exit pupil, where the electric field $\boldsymbol{E}_{\text{ex}}$ is given by

$$\boldsymbol{E}_{\mathrm{ex}}(\alpha_{\mathrm{en}},\beta_{\mathrm{en}},\gamma_{\mathrm{en}})=\frac{r_{\mathrm{en}}\cdot\alpha_{\mathrm{en}}}{r_{\mathrm{ex}}\cdot\alpha_{\mathrm{ex}}}\cdot\sqrt{\frac{\gamma_{\mathrm{in}}}{\gamma_{\mathrm{ex}}}}\cdot\boldsymbol{T}_{\mathrm{ex}}\cdot\boldsymbol{E}_{\mathrm{en}} \tag{S16}$$

$\boldsymbol{T}_{\mathrm{ex}}$ is the transformational matrix from the local exit pupil coordinates to the global image plane coordinates, which can be expressed as

$$\boldsymbol{T}_{\mathrm{ex}}=\begin{bmatrix} \frac{\beta_{\mathrm{ex}}}{\sqrt{1-\gamma_{\mathrm{ex}}^2}} & \frac{\alpha_{\mathrm{ex}}\cdot\gamma_{\mathrm{ex}}}{\sqrt{1-\gamma_{\mathrm{ex}}^2}} \\ \frac{\alpha_{\mathrm{ex}}}{\sqrt{1-\gamma_{\mathrm{ex}}^2}} & \frac{\alpha_{\mathrm{ex}}\cdot\gamma_{\mathrm{ex}}}{\sqrt{1-\gamma_{\mathrm{ex}}^2}} \\ 0 & \sqrt{1-\gamma_{\mathrm{ex}}^2} \end{bmatrix} \tag{S17}$$

Finally, the light wave is focused by the lens L3, yielding the resultant field distribution at the imaging plane:

$$\begin{aligned}\boldsymbol{E}_{\mathrm{img}}(x_{\mathrm{img}},y_{\mathrm{img}},z_{\mathrm{img}})=i\,&\frac{n\cdot\alpha_{\mathrm{en}}\cdot\exp(-i\cdot k\cdot r_{\mathrm{ex}})\cdot r_{\mathrm{ex}}}{\lambda\cdot\alpha_{\mathrm{ex}}}\cdot\\ &\iint\boldsymbol{E}_{ex}(\alpha_{\mathrm{ex}},\beta_{\mathrm{ex}},\gamma_{\mathrm{ex}})\cdot\exp(j\cdot k\cdot(\alpha_{\mathrm{ex}}\cdot x_{\mathrm{img}}+\beta_{\mathrm{ex}}\cdot y_{\mathrm{img}}))\frac{d\alpha_{\mathrm{ex}}\cdot d\beta_{\mathrm{ex}}}{\gamma_{\mathrm{ex}}}\end{aligned} \tag{S18}$$

S5. Temperature dependence of defect inspection

To evaluate whether a specific temperature increment is required for observable signal enhancement, we numerically investigated the dependence of defect inspection contrast on the pump-excitation temperature. The simulation configuration follows the same structure parameters and imaging conditions used in the Fig 3b, with the only varying parameter being the temperature of the silicon nanostructure. In the simulation, the temperature was varied from 25 °C to 800 °C, and the corresponding scattering fields were calculated using temperature-dependent optical constants of silicon. The resulting contrast values are plotted as a function of

temperature in Fig. S5a. The defect contrast increases significantly once the temperature reaches approximately 200 °C, indicating that photothermal modulation can effectively enhance defect detectability at a low temperature level. Moreover, strong contrast enhancement persists over a relatively broad temperature range from 200 °C to 600 °C. This behavior indicates that the SPM^2 mechanism does not require a strictly defined temperature increment, and the detectability enhancement depends on the magnitude of resonance modulation induced by the thermo-optic effect. As long as the product $(dn + dk)/dT \cdot dR/d\lambda$ is sufficiently large, measurable signal enhancement can be achieved. These results suggest that SPM^2 is tolerant to variations in the thermal excitation level and can maintain enhanced defect contrast within a relatively wide temperature range.

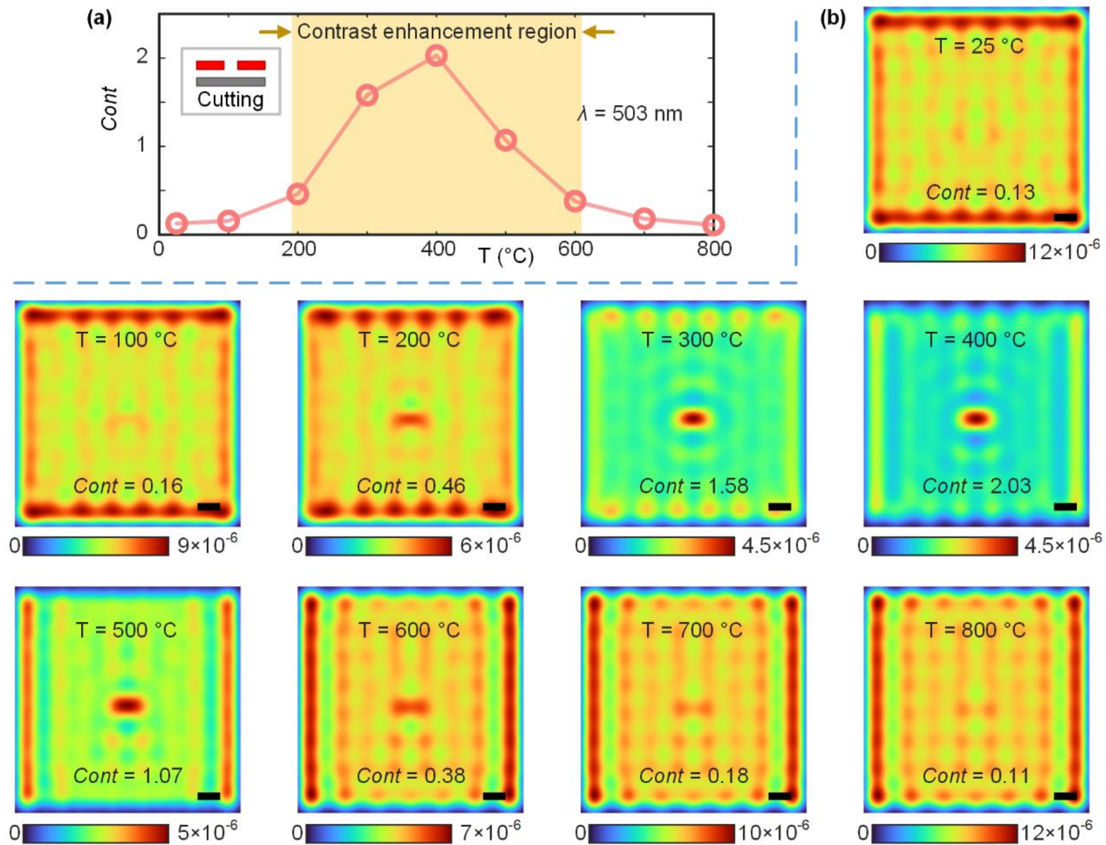

Figure S5. Simulated defect inspection under different excitation temperatures. (a) Calculated inspection contrast versus temperature. (b) Simulated initial far-field images of the IDA array at representative temperatures. scale bar: 1 μm.

S6. Photograph of the experimental photothermal-enhanced defect inspection setup

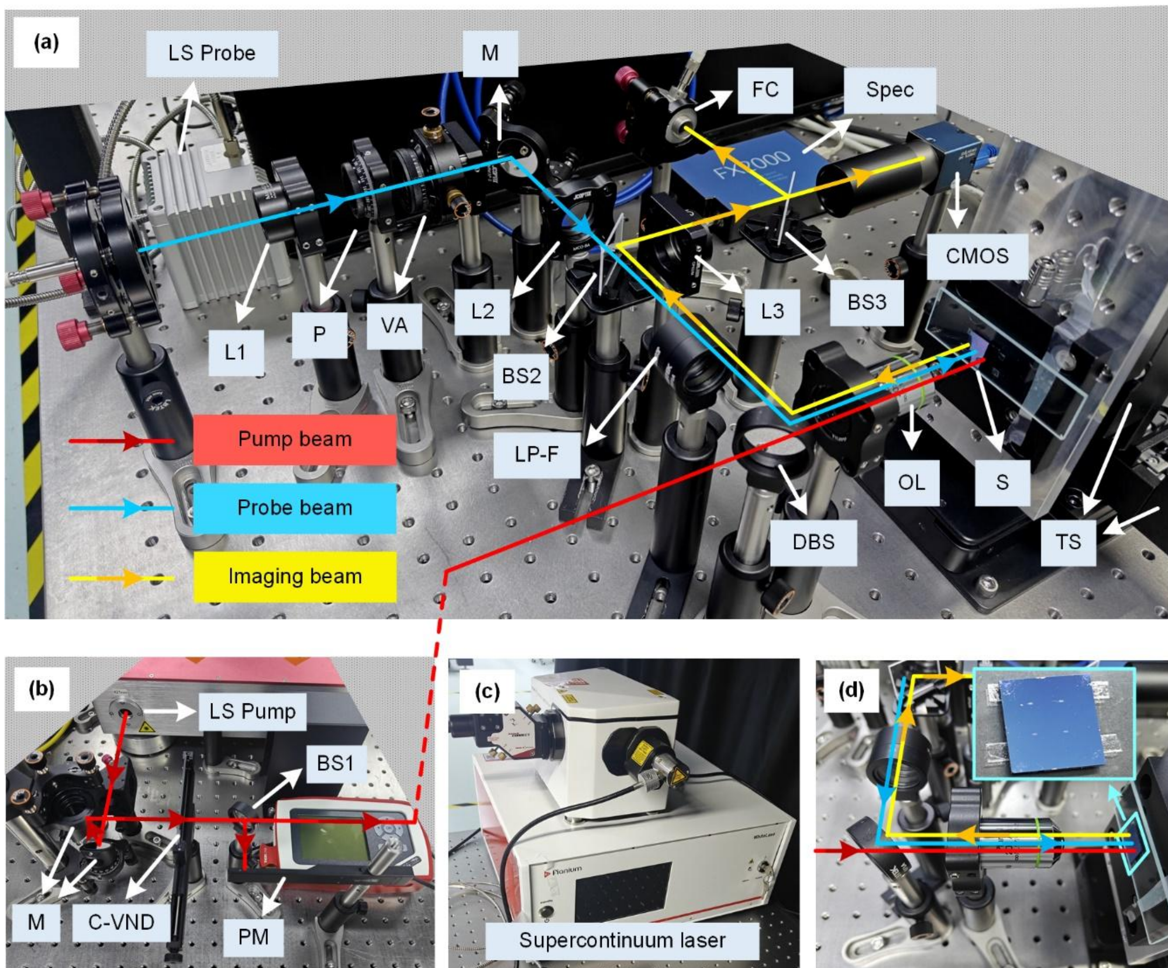

Figure S6. Photograph of the SPM² prototype. (a) Full view of the experimental prototype. (b) Pump power control with a C-VND filter and power meter (PM). (c) A super-continue laser provides the monochromatic probe beam. (d) Home-fabricated sample.

The experimental setup of the SPM^2 prototype is illustrated in Fig. S6a. The sample is illuminated in a wide-field Köhler configuration with a broadband white-light source, and the probe-beam is conditioned by a linear polarizer (P) and a variable aperture (VA). In the imaging path, we use a reflection mode with a 20X/0.4 NA objective. The imaging-beam is split by a beam splitter (BS3) and directed to both a CMOS camera for far-field imaging and a spectrometer (Spec) for reflectivity measurement. For far-field imaging, the probe-beam is provided by a supercontinuum laser, as shown in Fig. S6b. The pump-beam power is controlled by a continuously variable neutral-density (C-VND) filter and monitored in real-time with a power meter (PM) (Fig. S6c). A home-fabricated sample used in the defect inspection experiments is shown in Fig. S6d.

S7. The flowchart for fabricating the patterned SOI wafer

The thickness of the SOI stack was precisely determined using a spectroscopic ellipsometer (RC2 XI, J.A. Woollam Inc.). Ellipsometric measurements were conducted across the wavelength range of 210 nm to 2500 nm. The spectral resolution was 1 nm for the 210 nm to 1000 nm range and 6 nm for the 1000 nm to 2500 nm range. Measurements were performed at incidence angles of 55° and 65°. By fitting the spectral curves of the ellipsometric parameters (amplitude ratio angle Ψ and phase difference Δ), the precise thicknesses of the top-silicon layer and the buried-oxide layer were determined (partial measurement results are shown in Fig. 5b)[8]. Fabrication of patterned SOI wafers began with dicing a 4-inch wafer into smaller pieces, followed by a standard cleaning procedure. An oxygen plasma pretreatment was then applied to activate the wafer surfaces. Next, a resist was spin-coated onto the SOI wafer, followed by soft bake, exposure, development, and fixing. The nanopattern transfer was performed by etching,

after which the resist was removed. Finally, the nanopattern was photographed using SEM. A flowchart illustrating these steps is shown in Fig. S7.

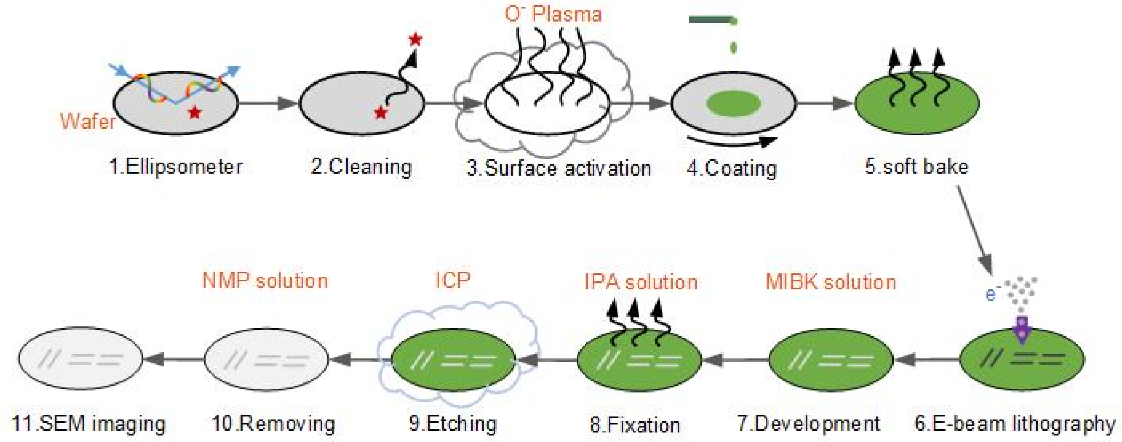

Figure S7. The flowchart for fabricating the patterned wafers.

S8. Experimental evaluation of pump-beam power density

The assessment of the pump-beam's average power density, I_{PD}, requires two critical parameters: the power delivered to the sample plane (P_2) and the size of the pump region (A). As shown in Fig. S8a, the pump-beam power is monitored in real time at Position 1 (P_1) using a PM. Due to the presence of BS1 and a DBS, the power measured at the monitoring position (P_1) differs from the power delivered to the sample plane (P_2). We shifted the C-VND filter and collected multiple power data sets at the monitoring position and the sample plane. The experimental data and the resulting linear fit are shown in Fig. S8b. The linear regression determines the relationship:

$$P_2 = 1.21 P_1 \text{ (mW)} \tag{S19}$$

where P_1 and P_2 are measured in mW.

To accurately determine the pump illumination region A on the sample, the pump spot was directly imaged. The long-pass filter (LP-F) was replaced with a neutral density filter (OFR1-

20M, JCOPTIX Inc.) and the probe-beam was turned off. With the pump power attenuated to a low level, the CMOS camera captured the intensity distribution of the pump-beam reflected from the sample. As shown in Fig. S8c, the recorded image reveals a primary circular spot accompanied by weak stray-light side lobes. The fitted diameter of the primary spot is approximately 10.5 µm. Image analysis further indicates that this primary spot contains approximately $\eta = 0.78$ of the total integrated energy. The peak power density at the center of the spot, denoted as $I_{\text{PD-max}}$, is measured to be 2.46 times the average power density $I_{\text{PD-avg}}$ over the primary-spot area. Accordingly, $I_{\text{PD-avg}}$ is defined based on the area of the primary spot as:

$$I_{\text{PD-avg}} = \frac{\eta \cdot P_2}{A} = \frac{0.78 \cdot 1.21 P_1}{\pi \cdot 5.25^2} \times 10^9 (\text{W m}^{-2}) \tag{S20}$$

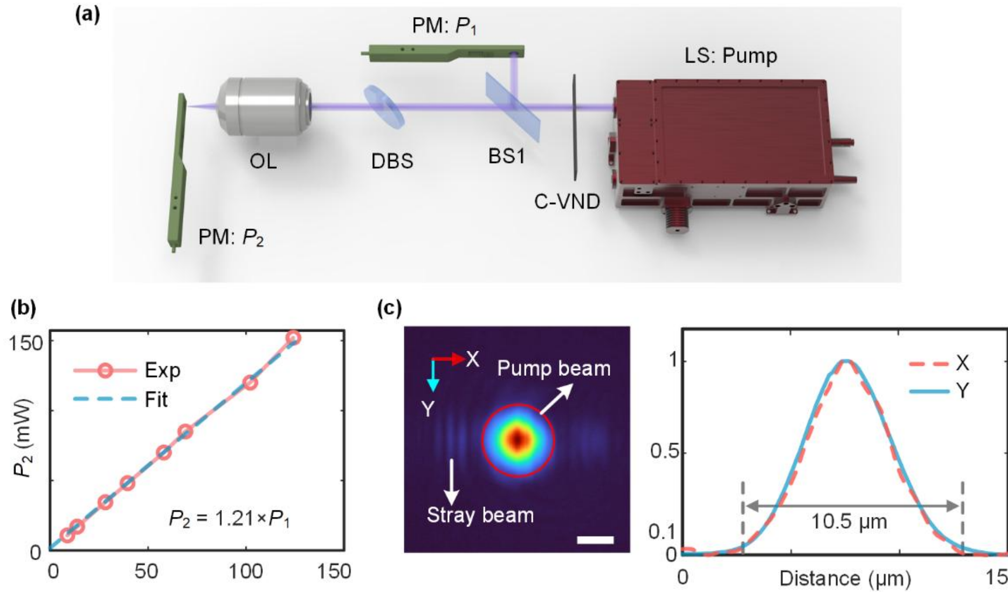

Figure S8. Experimental evaluation of the pump-beam power density. (a) Schematic diagram of the experimental setup. (b) Experimental data and linear fit of the monitored power P_1 and the power at the sample plane P_2. (c) Direct imaging of the pump-beam on the sample surface. The far-field image and corresponding intensity profile reveal a primary circular spot with a fitted diameter of approximately 10.5 µm. Scale bar: 5 µm.

S9. SEM verification of structural integrity after pump-excitations

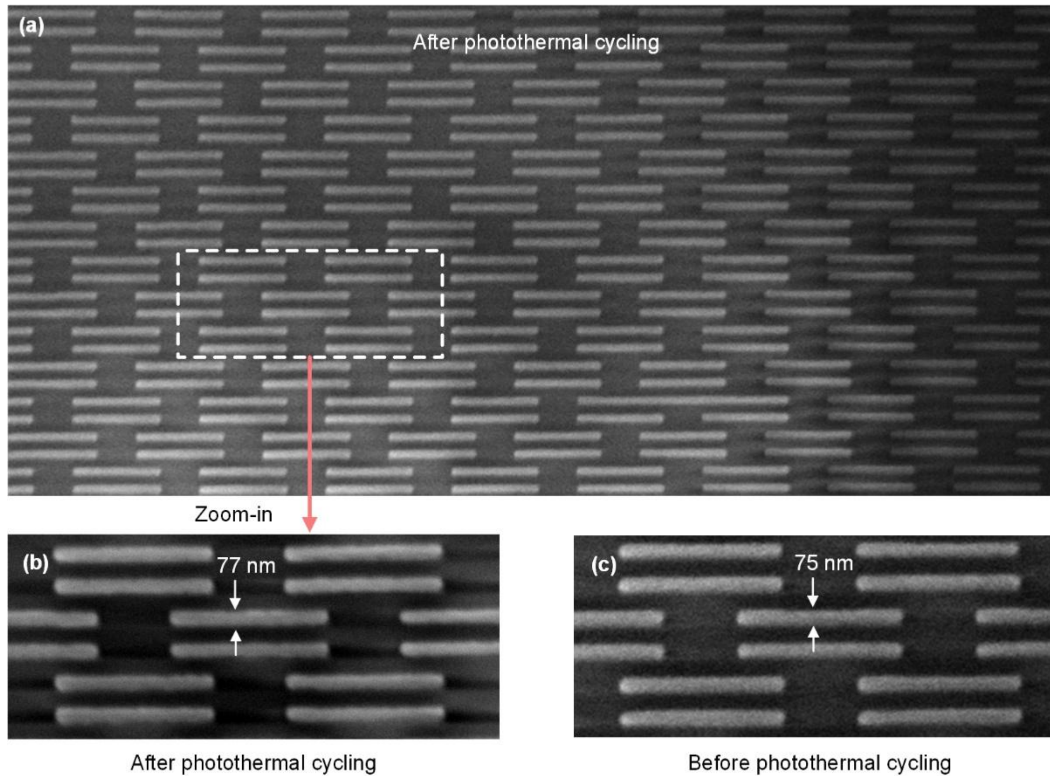

Figure S9 SEM verification of nanopattern stability. (a) SEM image of the nanopattern after 25 pump-excitation cycles (2 s pump-on followed by 2 s pump-off). (b) Magnified view of the region in (a). (c) SEM image of the nanopattern before pump excitation.

To evaluate the structural stability of the nanopattern under repeated pump-excitation, the sample shown in Fig. 6b-c was subjected to 25 excitation cycles, each consisting of 2 s pump-on followed by 2 s pump-off. This corresponds to a total pump exposure time of 50 s, far longer than that used during a single imaging measurement. The SEM characterization of the nanopattern after the excitation cycles is presented in Fig. S9a, with a magnified view shown in Fig. S9b. The nanostructures remain clearly visible and maintain their structural integrity. By

comparison with the initial SEM image before pump-excitation (Fig. S9c), no observable changes in nanowire morphology or edge roughness are detected. These results indicate that no cumulative thermal damage, such as melting or plastic deformation, occurs under the experimental pump conditions.

S10. Stitched scanning and contrast enhancement under non-uniform thermal conditions

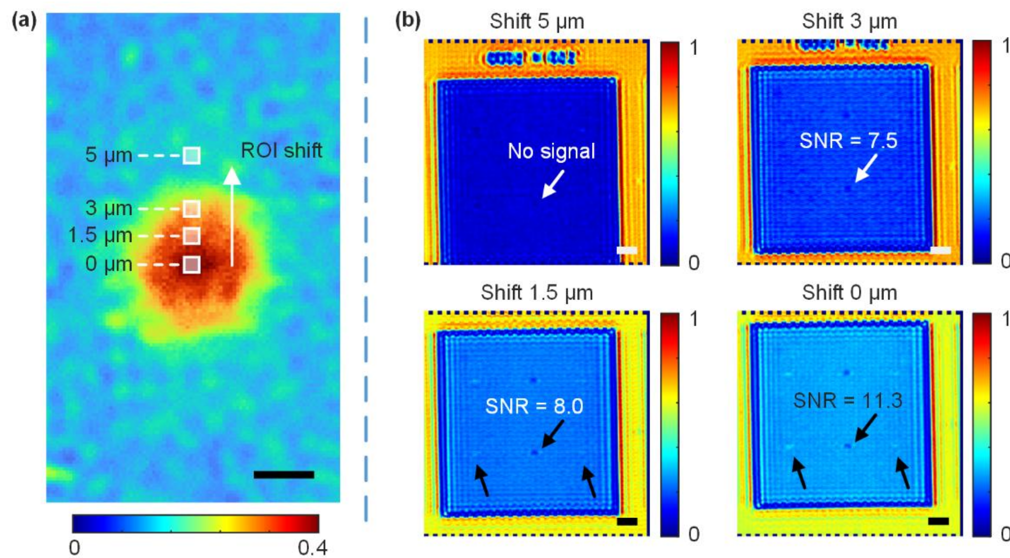

Figure S10. Defect inspection under different Pump power densities. (a) Schematic of the ROI Offset. Four offset distances of 0 μm, 1.5 μm, 3 μm, and 5 μm of the ROI relative to the center of the pump region. The 5 μm offset region represents the 25 °C inspection condition. (b) The stitched far-field images for different ROI offsets. As the ROI shifts from the outer to the inner of the pump, the far-field intensity of the nanopattern and the defect-perturbation signal are progressively enhanced. The SNR of the cutting defect for each offset is annotated in the stitched images. Defect signals are clearly visible at offsets of 1.5 μm and 0 μm. Scale bar: 4 μm.

To achieve large-area defect inspection, we employed a motorized stage for stitched-scanning imaging. The prototype's spatial sampling resolution in the sample plane is a critical parameter for determining the scanning step size. Based on the nominal objective focal length 9 mm and the actual tube lens L3 focal length 200 mm, the effective magnification is M = 200/9 ≈ 22.22. With a pixel size of 3.45 μm of the CMOS camera, the corresponding sampling resolution in the sample plane is

$$R_{samp} = \frac{3.45}{22.22} \approx 0.155 \text{ (μm pixel}^{-1}\text{)} \quad \text{(S21)}$$

Given the motorized stage's minimum step size of 0.1 μm, we set the scanning step size to 0.6 μm. This step size is approximately 4 times the sample-plane sampling resolution, ensuring sufficient pump-region overlap and minimizing stitching errors caused by non-integer sampling ratios.

The pump-beam intensity profile at the sample plane is typically non-uniform (e.g., Gaussian), resulting in a non-uniform excited thermal field. In the stitched images shown in Fig. 6c and 6d, the effective region of interest (ROI) for each scanning frame was set to the center of the pump region to ensure uniform enhancement. To analyze the defect inspection results under varying local pump power densities, we intentionally shift the ROI during scanning. As depicted in Fig. S10a, we used four shift distances: 0 μm, 1.5 μm, 3 μm, and 5 μm. The 0 μm shift corresponds to the maximum power density at the center of the pump region. In contrast, the ROI with a 5 μm shift lies near the edge of the excited region, where the photothermal excitation is minimal. No measurable change in the scattering signal is observed at this position, making it effectively equivalent to the 25 °C inspection condition of BFI. As shown in Fig. S10b, as the ROI offset decreases from 5 μm to 0 μm, the far-field image intensity increases, and the defect-perturbation signal becomes more pronounced. In the stitched images for the 1.5 μm and 0 μm offsets, the

perturbation signals generated by all six defects (Fig. 6c) are clearly visible. Quantitative SNR (defined in S11) analysis of a cutting defect confirms this trend: at offsets of 5 μm, 3 μm, 1.5 μm, and 0 μm, the measured SNR values are undetectable (<2), 7.5, 8.0, and 11.3, respectively. This result further indicates that SPM² does not require a specific thermal condition; as long as the photothermal effect induces measurable scattering-field modulation, enhanced defect inspection sensitivity can be achieved.

In terms of inspection throughput, based on the effective scattering modulation region of approximately 8 μm in diameter, which defines the area where photothermal enhancement is experimentally observed, and a camera integration time of 20 ms, the current prototype achieves an inspection rate of ~2500 μm^2 per second. However, for generating stitched images with 0.6 μm step size, the effective throughput is approximately 18 μm^2 per second. We acknowledge that this throughput is modest compared to industrial BFI systems, as the pump-excitation is confined to a small region under the critical illumination configuration used in our proof-of-concept setup. However, this limitation is engineering-based rather than fundamental: the microsecond-scale thermal dynamics (Fig. 2l) do not constrain imaging speed, and with a suitable high-power, low-coherence source engineered for wide-field excitation, the method can achieve throughput comparable to conventional BFI.

S11. Experimental signal-to-noise ratio analysis of defect perturbation signals

To quantitatively evaluate the defect detectability in the experimental results shown in Fig. 6, a signal-to-noise ratio (SNR) analysis was performed to the second-order self-differencing images. Because the inspected nanostructures are periodic, the periodic background scattering field can be effectively removed by applying second-order self-differencing:

$$D(m,n) = I(m,n+p\cdot i) - 2\cdot I(m,n) + I(m,n-p\cdot i) \tag{S22}$$

Here, D refers to the second-order differential image. The period of the nanopatterns, expressed in pixels, is denoted as p, with I representing the shift step index. The horizontal and vertical pixel coordinates are indicated by m and n, respectively. The SNR is defined as the ratio between the maximum defect-induced perturbation signal I_{Pert} in the differential image and the standard deviation (σ) of the background signal in a defect-free region I_{Bg}, which is expressed by:

$$SNR = \frac{\max(I_{\text{Pert}})}{\sigma(I_{\text{Bg}})} \tag{S23}$$

Figs. S11a and S11b correspond to the same test IDA pattern and inspection configuration as in Fig. 6c. For the Bx-bridge defect located on the left side, the SNR decreases from 9.7 at 25 °C to 1.9 under pump-on conditions, indicating that the Bx-bridge defect changes from detectable to undetectable. In contrast, the cutting defect in the middle region shows an enhancement, with the SNR increasing from 1.3 at 25 °C to 5.9 under pump-on condition, demonstrating that the defect becomes detectable under thermal excitation. These contrasting results demonstrate that defect type significantly influences both baseline detectability and the response to photothermal modulation, with different defects exhibiting opposite enhancement behaviors.

A distinct contrast pattern emerges in Figs. S11c and S11d, which correspond to the same configuration as Fig. 6d. Under pump-excitation, all three types of defects become visible (SNR: 8.3, 11.3, and 5.7), whereas they are undetectable at room temperature. Notably, the Bx-bridge defect exhibits strong enhancement in Fig. S11c, which is suppressed in Fig. S11a. This contrast reversal indicates that the effectiveness of photothermal enhancement is influenced by multiple factors, including defect size, background pattern dimensions, and the probe wavelength. These results quantitatively confirm that the proposed SPM^2 mechanism can significantly improve

defect detectability by enhancing defect-induced perturbation signals relative to background noise.

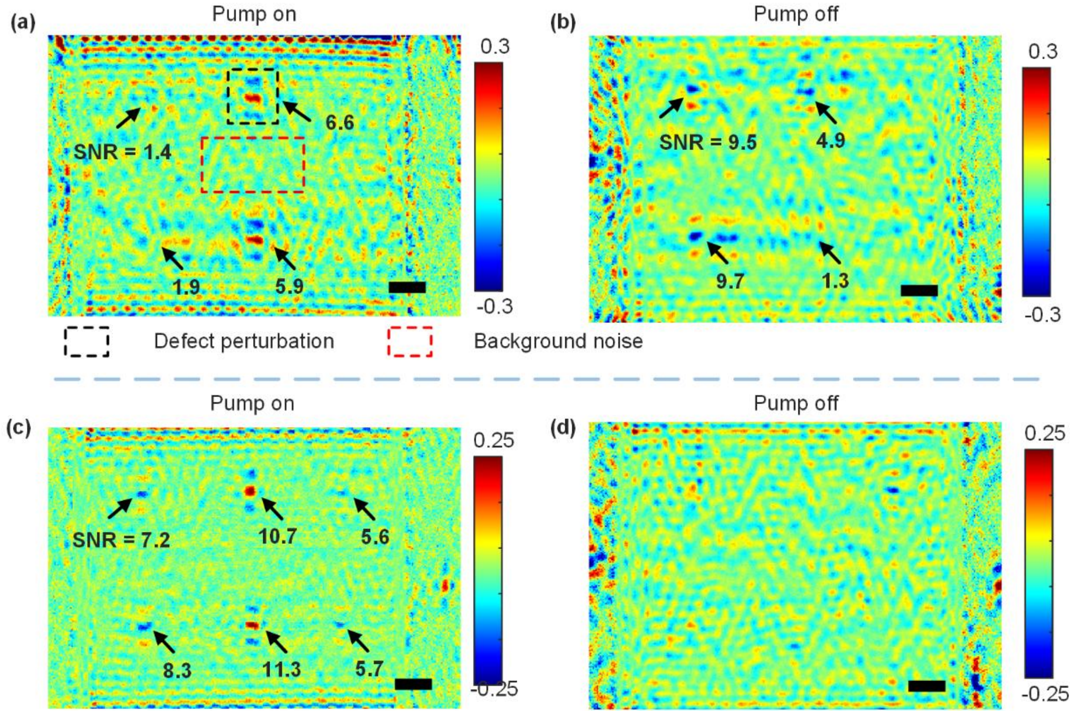

Figure S11. Experimental self-differential images and SNR analysis of defect perturbation signals. (a) Self-differential image under pump-excitation. (b) Self-differential image without pump-excitation. (a) and (b) correspond to the same sample and inspection configuration as in Fig. 6c. (c) Self-differential image under pump-excitation. (d) Self-differential image with the pump turned off. Panels (c) and (d) correspond to the same sample and inspection configuration as in Fig. 6d. Scale bar is 4 μm.

Reference

1. Jellison, G. E., Jr. & Modine, F. A. Optical functions of silicon at elevated temperatures. *Journal of Applied Physics* **76**, 3758-3761 (1994).

2. Jellison, G. E., Jr. & Burke, H. H. The temperature dependence of the refractive index of silicon at elevated temperatures at several laser wavelengths. *Journal of Applied Physics* **60**, 841-843 (1986).

3. Bohren, C. F. & Huffman, D. R. Absorption and Scattering by an Arbitrary Particle. In: *Scattering, Absorption, and Emission of Light by Small Particle*). Cambridge University Press (1998).

4. Yang, P. & Liou, K. N. Finite-difference time domain method for light scattering by small ice crystals in three-dimensional space. *Journal of the Optical Society of America A* **13**, 2072-2085 (1996).

5. Kononchuk, O. & Nguyen, B.-Y. *Silicon-on-insulator (soi) technology: Manufacture and applications*. Elsevier (2014).

6. Huang, Z. *et al.* Thermal conductivity of amorphous and crystalline thin films by molecular dynamics simulation. *Physica B: Condensed Matter* **404**, 1790-1793 (2009).

7. Shen, Y. Level-set based mask synthesis with a vector imaging model. *Optics Express* **25**, 21775-21785 (2017).

8. Liu, S. *et al.* Development of a broadband Mueller matrix ellipsometer as a powerful tool for nanostructure metrology. *Thin Solid Films* **584**, 176-185 (2015).